Hindawi
International Journal of Corrosion
Volume 2021, Article ID 8833346, 13 pages
https://doi.org/10.1155/2021/8833346

Research Article

Effect of Alternating Stray Current Density on Corrosion Behavior of X80 Steel under Disbonded Coating

Qing-Miao Ding,[1] Yong-Xiang Qin,[1] Tao Shen,[2] and Yu-ning Gao[1]

[1]*Aeronautical Engineering Institute, Civil Aviation University of China, Tianjin 300300, China*
[2]*College of Computer Science and Technology, Civil Aviation University of China, Tianjin 300300, China*

Correspondence should be addressed to Qing-Miao Ding; qmding@cauc.edu.cn and Yong-Xiang Qin; 550462668@qq.com

Received 18 September 2020; Accepted 18 May 2021; Published 28 June 2021

Academic Editor: Flavio Deflorian

In this paper, the effect of alternating stray current (AC) density on the corrosion behavior of X80 steel under disbonded coating was studied by electrochemical methods, wire beam electrode (WBE) technology, and surface observation technology. The results showed that under the interference of different AC densities, the corrosion potential of X80 steel under disbonded coating underwent negative deviation, and the degree of negative deviation increased with the increase of AC density. The corrosion current density of X80 steel under disbonded coating with the action of 0~100 A/m^2 AC density had few differences. While the corrosion current density of X80 steel with the action of 200~300 A/m^2 AC density increased and the corrosion current density was higher than that under low AC density. The cathode area of the wire beam electrode under disbonded coating is mainly distributed outside and the edge of the gap between disbonded coating and X80 steel, while the anode area is mainly distributed inside the gap.

1. Introduction

At present, the most common anticorrosion measure of buried pipeline was the combination of anticorrosion coating and cathodic protection. However, the coating was inevitably mechanically damaged during usage or transportation. At the same time, the pipeline would be corroded by the surrounding medium during its service, which would inevitably lead to defects such as peeling of the coating [1–3]. The AC stray current flowed in or out at the defects of the pipeline anticorrosion coating, which directly accelerated the corrosion and destruction of the metal [4, 5]. It also generated AC power in the metal pipeline by induction, which further accelerated the corrosion and destruction of the pipeline and greatly shortened the service life of the pipeline. Studies have shown that the metal corrosion mechanism under the release coating was similar to that of metal crevice corrosion [6–10]. At present, most people were more aware of the autocatalytic acceleration theory of the occlusion cell proposed by Ahmad [11] and the IR potential drop theory of Pickering [12]. Williford et al. used a rectangular slot device to influence the corrosion of 2Cr13 stainless steel [13]. The results showed that the high-temperature environment promoted the negative movement of the self-corrosion potential of the metal, which increases the probability of crevice corrosion of 2Cr13 steel. Huo [14] studied the effects of HCO_3^- and SO_4^{2-} on the corrosion behavior of X70 steel under coating defects. The results showed that when the concentration of Cl^- in the solution was constant, the corrosion degree of X70 steel increased with the increase of HCO_3^- concentration. First, decrease and then increase the trend. Yan et al. studied the characteristics of the electrochemical environment of the slit thin liquid under the disbonded coating [15]. At high pH, O_2 entered the gap and contributed to the passivation of the metal. Wen et al. studied the corrosion law of X70 steel in the crack gap and focused on the analysis of the pH value in the experimental solution [16]. The results showed that under certain conditions, the pH value in the solution environment had a significant effect on the degree of metal offset at the bottom of the gap. Zhu et al. found that AC interference can lead to pitting corrosion of X80 steel, and the SCC sensitivity of steel increased with the increase

Table 1: Chemical composition of X80 steel (wt%).

C	Si	Mn	Cr	Mo	Ni	Al	Cu	Nb	Ti	Pb	Fe
0.042	0.189	1.560	0.028	0.243	0.230	0.034	0.153	0.060	0.019	0.005	Margin

of AC current density at the pit and coating stripping [17]. Bosch and Bogaerts selected 0.02 mol/L NaCl solution and 0.5 mol/L Na_2CO_3+1 mol/L $NaHCO_3$ solution to study the effect of solution conductivity on the corrosion behavior of metal under the peeling coating and obtained the potential gradient of the metal in the seam [18]. As the conductivity of the solution increased, the cathodic protection depth of the metal in the slit gradually increased. Li et al. studied the effect of cathodic polarization on buried pipeline steel in the stripping zone. The results showed that the protective distance in the stripping gap increased with the negative shift of the slit protection potential [19]. The influence of AC stray current on the corrosion behavior of metal under the peeling coating defect was more. At present, domestic and foreign scholars had relatively little research on the influence of different AC stray current density on the corrosion of metal under the peeling coating defect. However, there were some differences in the AC density for the actual laying environment of the pipeline. Therefore, studying the influence of different stray current densities on the corrosion behavior of the metal under the stripping coating was of great significance for the actual safe operation of the pipeline.

In this paper, by analyzing the Eocp of X80 steel, the corrosion current density, and the potential current at different positions of the array electrode, the effects of different AC current intensity interference on the corrosion rate of X80 steel and the distribution of cathode and anode regions under the defect of peeling coating were studied, in order to provide a certain theoretical basis for practical engineering applications.

2. Experimental

2.1. Experimental Preparation

2.1.1. Electrochemical Test Electrode. Electrochemical test electrodes were selected from X80 pipeline steel with dimensions of 50 mm × 25 mm × 2 mm, and water-grinding papers of different grits (up to 2500) were used for progressive fine grinding in a staggered direction. The chemical composition (wt%) of the X80 pipeline steel is shown in Table 1 [20, 21]. Subsequently, ultrasonic cleaning was carried out in deionized water and absolute ethanol of 100 mL for 10 minutes. We attached a 0.5 mm thick gap gasket and a 46 mm × 25 mm plexiglass plate on the X80 steel polished working surface and soldered the copper wire on the other side of the polished surface. The gap between the X80 steel polished working surface, and the plexiglass plate was used to simulate the peeling zone between the disbonded coating and the pipeline metal substrate. The gasket was used to adjust the gap height dimension. The sample was sealed with polytetrafluoroethylene (PTFE) to form a sheet sample having a peeling height of 0.5 mm and a damaged area of 1 cm^2, as shown in Figure 1.

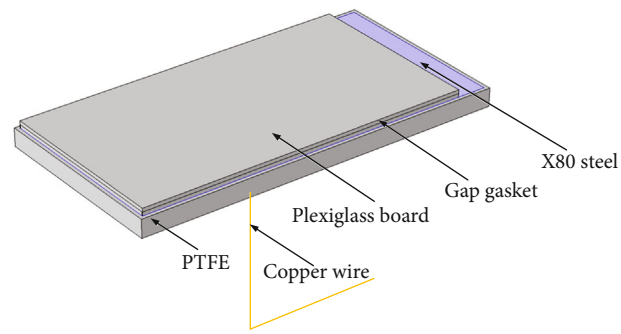

Figure 1: Electrochemical test electrode schematic.

2.1.2. Array Electrode. The plexiglass plate was a machined plate with small holes of 10 × 10 array with a diameter of 2 mm. The X80 wires with a diameter of 2 mm were put into the small holes on the plexiglass plate and then cast with epoxy resin and cured at room temperature for usage. After being ground, degreased, dewatered, and dried, the array electrode was attached to the other plexiglass plate of 30 mm × 30 mm. The surface formed a gap space with a peeling height of 0.5 mm [22]. The gasket was used to adjust the gap height dimension. The schematic diagram of the array electrode is shown in Figure 2. The X indicated the column of the array electrode, that was, the number of columns increased with the arrow points. The Y indicated the row of the array electrode, that was, the number of rows increased with the arrow points. The point (X, Y) represented X column and Y row. The damage points were from point (1) to point (1, 10), which was the first line of the array electrode and represented the points outside the gap. We divided the study areas into outside, edge, inside, and bottom of the gap according to the distance from the location of the damage point.

2.1.3. Experimental Medium. The simulated soil solution could reflect the real soil corrosion, reduced the test error caused by the different water absorption rate of the soil, and accelerated the corrosion. Therefore, the soil simulation solution was selected for the experimental study. The soil simulated solution used in the experiment was taken from the soil around a certain oil pipeline, and it was centrifuged to obtain the chemical composition and substance content as shown in Table 2 [23].

2.2. Experimental Device and Methods

2.2.1. Electrochemical Testing. The working electrode was immersed in the soil simulation solution, and a sine wave signal was applied with a signal generator. The frequency was set to 50 Hz, wherein the AC density [24] was 0 A/m^2, 30 A/m^2, 50 A/m^2, 100 A/m^2, 200 A/m^2, and 300 A/m^2. One end of the AC signal was connected to the carbon rod and

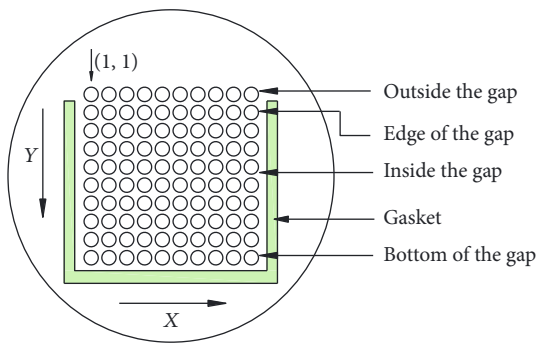

(a) Electrode dot distribution of array electrodes

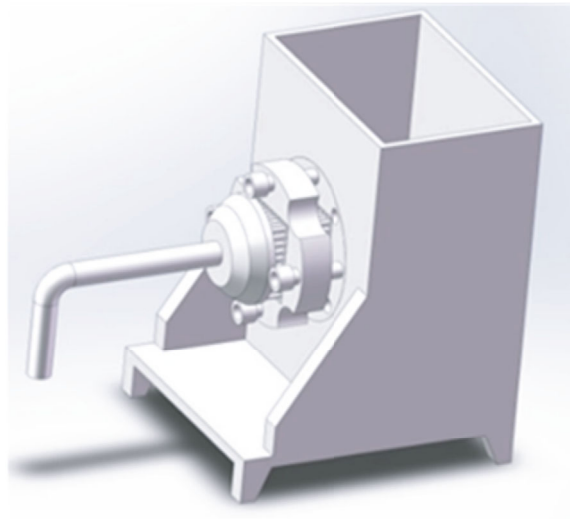

(b) Schematic diagram of the appearance of the array electrode

Figure 2: Array electrode schematic.

Table 2: Composition of soil simulated solution.

Ingredient	H_2O	Na_2CO_3	NaCl	Na_2SO_4	$NaHCO_3$
Content	1000 mL	0.1600 g	0.5125 g	0.1712 g	0.0865 g

inserted into the simulated solution, and the other end was connected to the working electrode. The three-electrode system was used to electrochemically test the working electrode of the coupon sample to obtain the open circuit potential (Eocp), electrochemical curves, and electrochemical impedance spectroscopy of the X80 steel under the disbonded coating defects. All the electrochemical tests were carried out using a CHI660d electrochemical workstation. The X80 steel specimen was used as the working electrode (WE), a large area platinum as the counter electrode (CE), and a saturated calomel electrode (SCE) as the reference electrode (RE). All potentials in the article were relative to the SCE reference electrode unless otherwise specified. To reduce the IR drop, RE was located 2 mm away from WE by a salt bridge. The series capacitor was used in the external circuit of the AC signal to prevent the DC electrochemical test system from interfering with the alternating current line. The series inductance method was adopted in the electrochemical test circuit to prevent the AC signal from interfering with the electrochemical test system. And the two circuits were independent of each other. The device schematic is shown in Figure 3.

2.2.2. WBE Test. The box containing the simulated solution was designed. When performing WBE measurement on the array electrode, the array electrode was used as the working electrode and the saturated calomel electrode was used as the auxiliary anode. Meanwhile, the array electrode was mounted on the side of the box, the array electrode working surface was immersed in the simulated solution, and the other end was connected to the tester through the probes. Otherwise, one end of the AC signal was connected to the

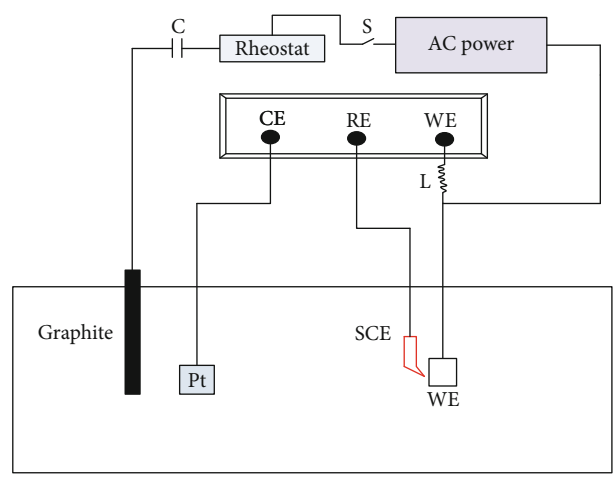

Figure 3: Electrochemical test device diagram.

carbon rod and inserted into the simulated solution, and the other end was connected to the array electrode. In order to obtain the potential and current distribution of the X80 steel inside and outside the gap under the disbonded coating defect, the working electrode to be tested was shorted to the opposite end of the zero-resistance current meter of the tow electrode current scanner, and another 99 electrodes ware grounded, and then they were switched one by one. The experimental test device is shown in Figure 4.

3. Results and Discussion

3.1. Open Circuit Potential. The corrosion potential of X80 steel changed with time under different AC current densities, as shown in Figure 5. Each curve was divided into three stages, 0~600 s was the potential of X80 steel with no AC interference, 600~1200 s was the potential of X80 steel under

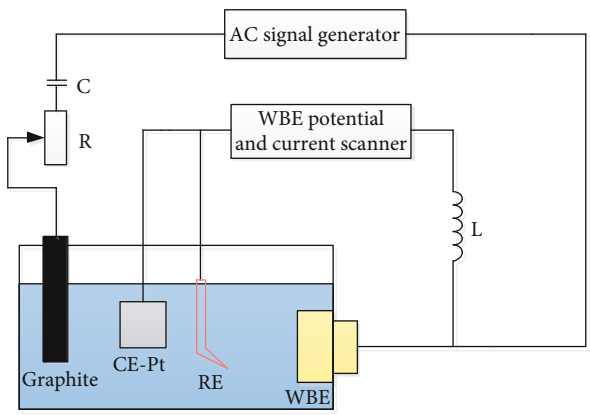

Figure 4: WBE test experimental device diagram.

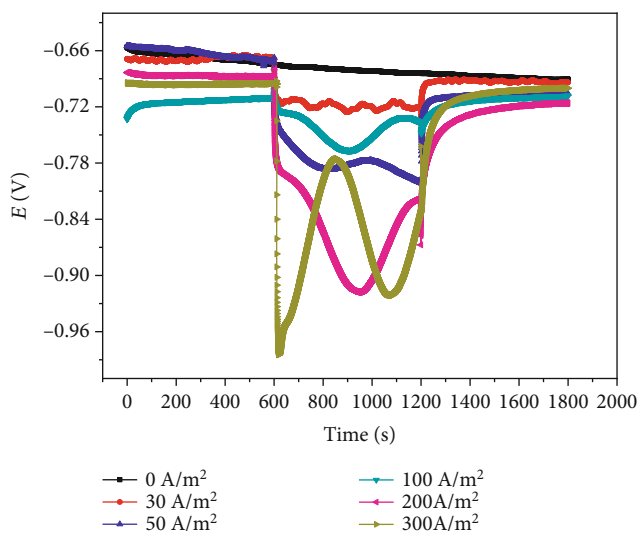

Figure 5: Eocp changes with time under different AC current density.

AC interference, and the last stage was the potential after removing the AC interference.

It could be seen from Figure 5, when no AC interference was applied, the potential of X80 steel was about -0.66 V, and it stabilized at -0.70 V as time gone on. At the moment (600 s) of applying AC interference, the potential of X80 steel had a certain negative shift, and the corrosion potential of X80 steel fluctuated as time gone on. As the AC current density increased, the fluctuation amplitude of the corrosion potential increased. This was because the AC interference caused the interface between metal and solution to be unstable and the voltage drop at the interface to change continuously [25]. The working area of X80 steel during the test was the same, so the AC current density was proportional to the voltage. It was known that as the AC current density increased, the instability of the interface increased, and the fluctuation amplitude of the corrosion potential increased. We calculated the corrosion potential offset ΔE (as shown in formula (1)) under different AC current density disturbances, and a function of ΔE as the AC current density is shown in Figure 6. It

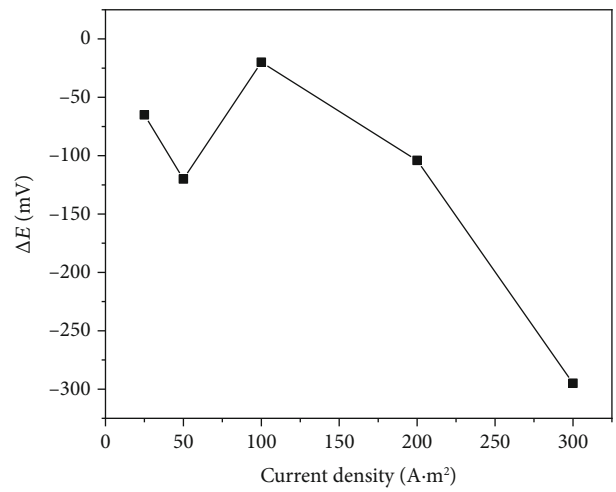

Figure 6: Corrosion potential offset of X80 steel under different AC densities.

could be found that the corrosion potential was negatively shifted, and it indicated that the application of AC interference did affect the working electrode potential, increased the electrochemical activity of the pipeline steel, and might accelerate the corrosion of the steel [26]. As the AC current density increased, the interface voltage drop between electrode and solution increased, and the potential difference between cathodic polarization and anodic polarization increased, so the negative offset of the Eocp of steel increased.

$$\Delta E = E_{\text{before}} - E_{\text{after}}, \tag{1}$$

where ΔE was the corrosion potential offset, E_{before} was the potential after interference, and E_{after} was the potential before interference.

Introducing a mathematical model [27]:

$$E_{\text{corr,AC}} = E_{\text{corr}} - \frac{b_a}{b_a/b_c - 1} \ln \left[\frac{\sum_{k=1}^{\infty} \left(1/(\text{k}!)^2\right) \left(E_{\text{p}}/2b_c\right)^{2k} + 1}{\sum_{k=1}^{\infty} \left(1/(\text{k}!)^2\right) \left(E_{\text{p}}/2b_a\right)^{2k} + 1} \right], \tag{2}$$

where $E_{\text{corr,AC}}$ was the AC interference corrosion potential, E_{corr} was the corrosion potential of X80 steel with no AC interference, b_a was the anode Tafel slope, b_c was the cathode Tafel slope, E_{p} was the peak potential of X80 steel with AC interference, and k was an integer. It could be seen from formula (2) that the change in corrosion potential caused by alternating current interference was a function of r ($r = b_a/b_c$) and E_{p}. When E_{p} increased, the corrosion potential shifted negatively. The direction of the offset depended on r, and only when $r \neq 1$, it would affect the corrosion of the metal. Since the electrode area was always constant during the test, the AC current density was proportional to the AC peak value, so the test conclusion was consistent with formula (2).

After the AC interference was removed, the potential of X80 steel with the low AC current interference before was

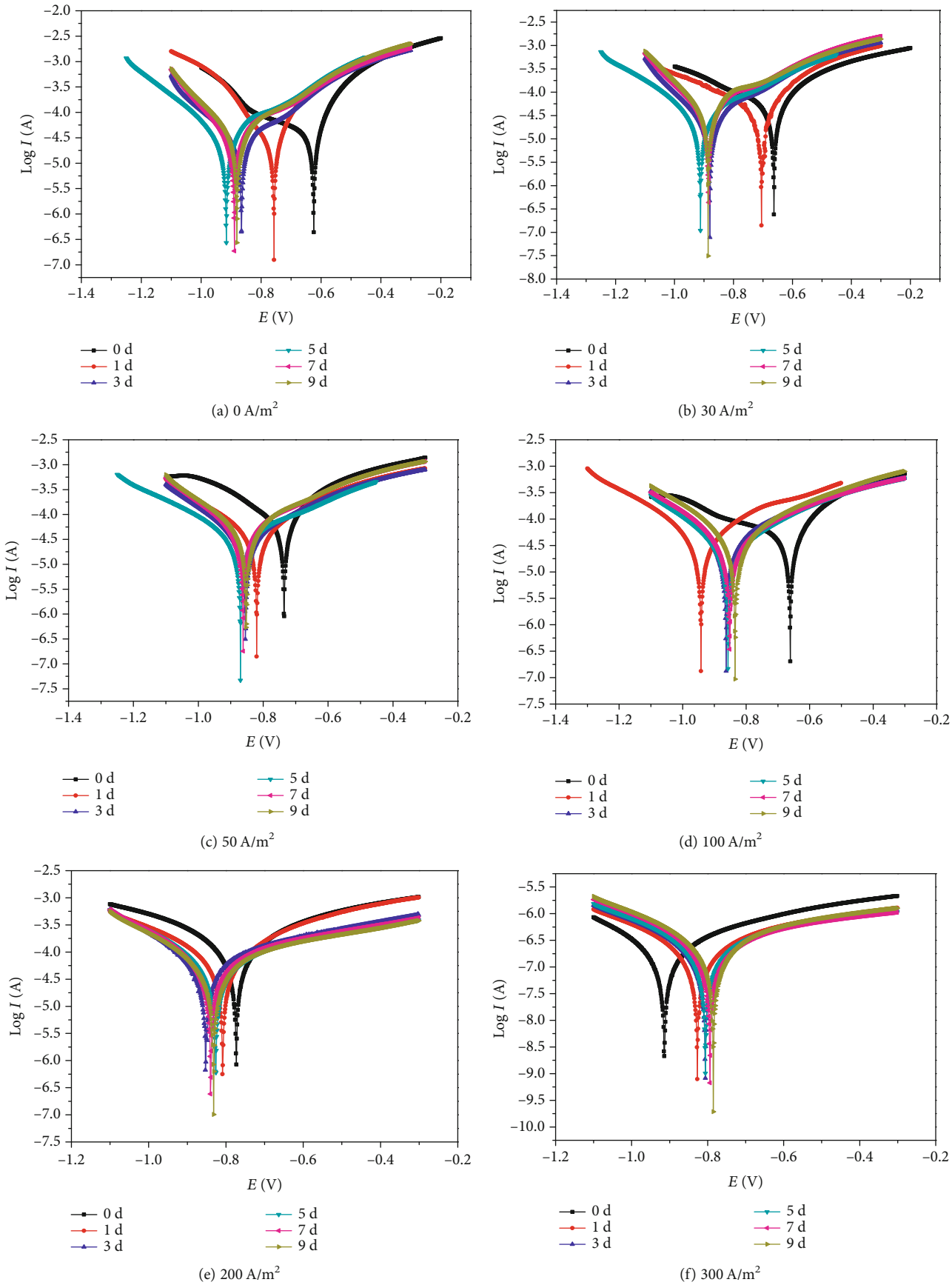

Figure 7: Polarization curves of X80 steel under different AC densities.

Table 3: Electrochemical parameters of polarization curves of X80 steel under different AC densities.

AC current density (A/m^2)	Time (d)	Corrosion potential (V)	Corrosion current density ($\mu A/cm^2$)	The ratio of anode to cathode Tafel slope
	0	-0.624	48.99	4.528
0	5	-0.916	23.94	1.193
	9	-0.881	40.32	0.824
	0	-0.663	65.69	1.938
30	5	-0.912	25.95	0.917
	9	-0.891	44.84	1.125
	0	-0.730	93.11	1.482
50	5	-0.870	34.99	0.975
	9	-0.882	40.20	0.947
	0	-0.661	66.83	2.910
100	5	-0.868	27.79	0.906
	9	-0.852	37.92	0.880
	0	-0.773	86.63	0.992
200	5	-0.826	46.60	0.760
	9	-0.832	43.15	0.737
	0	-0.914	90.38	0.876
300	5	-0.798	56.82	0.850
	9	-0.785	61.89	0.842

closer to the potential with no AC current before, but the potential of X80 steel with the AC current interference before was still lower than the potential of X80 steel with no current interference. It showed that the phenomenon of enhanced corrosion after AC removal would continue, and it further explained the irreversibility of AC corrosion [28].

3.2. Polarization Curves. The polarization curves of X80 steel with different AC interference are shown in Figure 7. The fitting electrochemical parameters of the polarization curves of X80 steel under different AC current densities are shown in Table 3.

It could be seen from Figure 7 that the application of the AC interference had a certain influence on the cathode and the anode of the metal, but the X80 steel under the disbonded coating was always in an active dissolved state, and no passivation occurred. The low of change of X80 steel corrosion potential with time under different AC current densities is shown in Figure 8. The corrosion potential was a measure of the thermodynamic trend of corrosion reactions in metals. In general, the more negative the corrosion potential of the metal, the greater the possibility of corrosion [29, 30]. It could be seen from Figure 5, Table 3, and Figure 8 that from the start of the test to the third day of the test, the corrosion potential changed sharply with time, and the potential gradient was as high as 300 mV and then gradually stabilized. The corrosion potential was positively shifted when the alternating current density was 300 A/m^2, while the corrosion potential was negatively shifted at the remaining current density. It indicated that the corrosion tendency of X80 steel increased

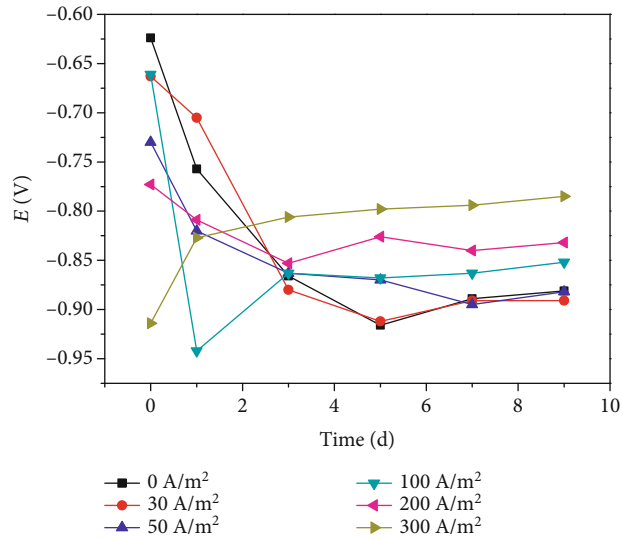

Figure 8: Variation of corrosion potential of X80 steel with time under different AC densities.

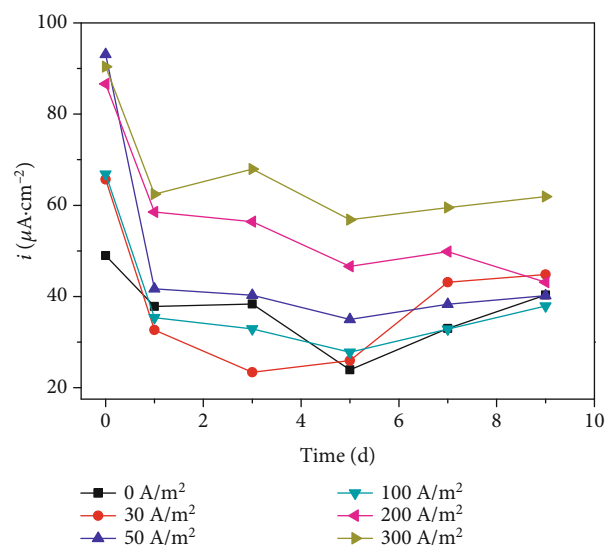

Figure 9: Correlation of corrosion current density with time under different AC densities.

significantly as the test progressed. There were two reasons for the negative shift of the corrosion potential after the superimposition of AC. On the one hand, the system supplemented the power consumed by the electrode reaction, thereby it indirectly accelerated the corrosion of the system, and the amount of electricity replenishment was proportional to the interference intensity. The corrosion potential was positively shifted [5] when the AC current density was 300 A/m^2. This was because the corrosion of X80 steel under strong AC interference was more serious than other conditions, it resulted in a large amount of corrosion products accumulating at the gap opening, and the corrosion tendency of X80 steel was weakened.

Figure 9 shows the corrosion current density of X80 steel with time under different AC densities. It could be seen that

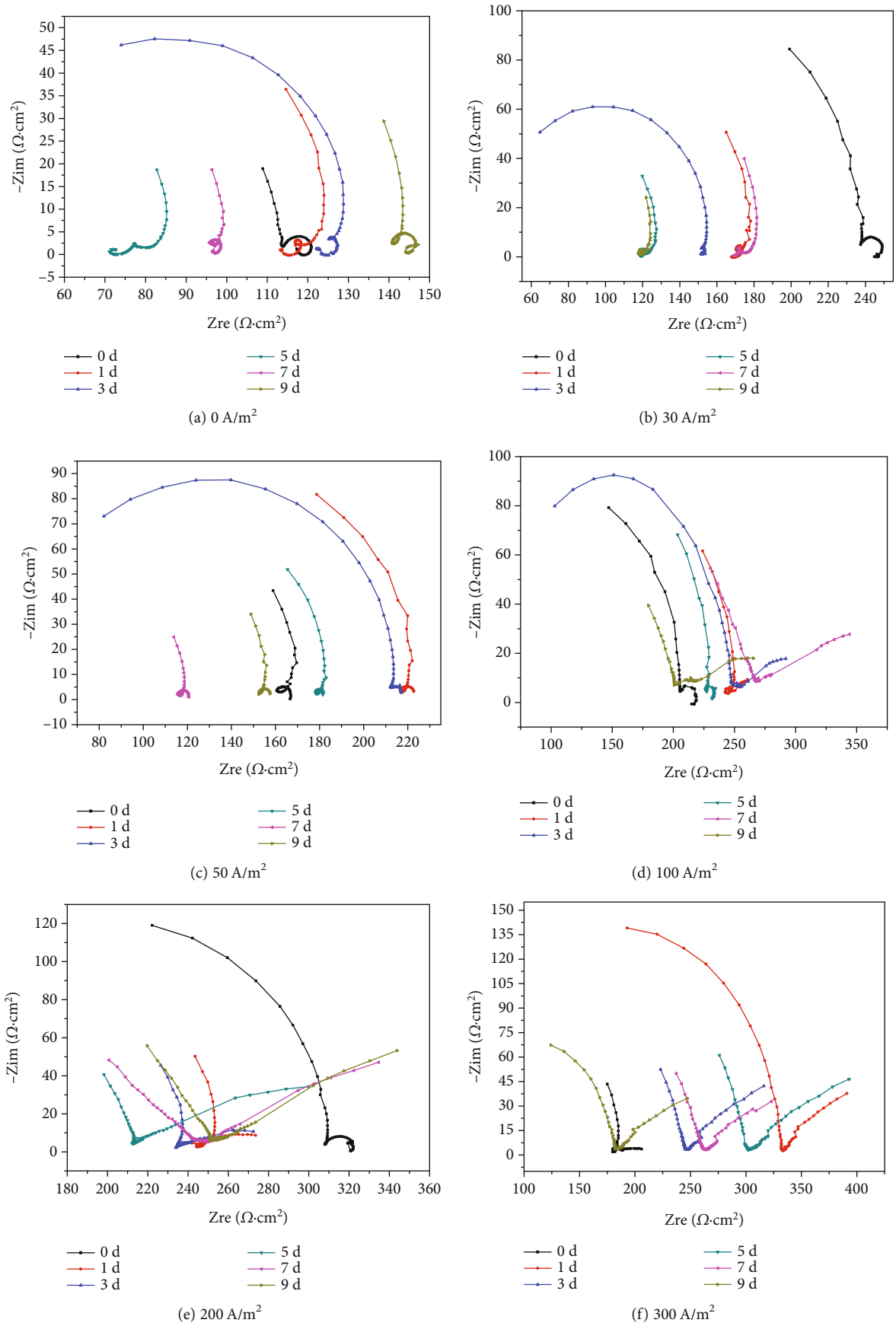

Figure 10: Electrochemical impedance spectroscopy of X80 steel with different AC densities.

the oscillation of the alternating current increased the electrochemical activity of the working electrode and accelerated the corrosion rate of the metal. And since the test has just started, the surface of the working electrode was clean and has no corrosive products and the oxygen content was relatively high, which was favorable for ion exchange, so the corrosion current density greatly increased. The corrosion current density cases decreased to some extent on the first day of the test, and the reductions were 11.18 μA/cm^2, 33.04 μA/cm^2, 51.42 μA/cm^2, 31.49 μA/cm^2, 28.12 μA/cm^2, and 27.96 μA/cm^2. It could be seen that the decrease of the corrosion current density increased first and then decreased with the increase of the AC density. When the AC interference was 50 A/m^2, the gradient of the corrosion current density decreased most. During the first 5 days of the test, the corrosion current density decreased to a certain extent from the beginning of the test and reached a minimum on the fifth day. This was because as the test progressed, oxygen was consumed and the corrosion products began to accumulate to some extent on the electrode. The accumulation of corrosion products at the damage point of the coating was particularly pronounced and visible to the naked eye. At this stage, the diffusion of oxygen and the accumulation of corrosion products worked together, resulting in a decreasing trend of corrosion current density. As the test progressed, the corrosion current density increased slightly. This was because the oxygen concentration difference became large, and the metal inside the slit and the metal outside the slit constituted an oxygen concentration cell, which accelerated the corrosion of the metal inside the slit, resulting in an increase in the corrosion current density.

On the 9th day of the experiment, the corrosion current density was 62 μA/cm^2 when the 300 A/m^2 AC interference was applied, and the corrosion current density was 40 μA/cm^2 under other interference conditions. Overall, when the applied AC stray current density was less than 100 A/m^2, the corrosion current density was not much different, and the fluctuation range was from 25 μA/cm^2 to 43 μA/cm^2. When the applied AC stray current density was more than 200 A/m^2, the corrosion current density increased as the interference current density increased, and it was higher than the corrosion current density under AC of 0~100 A/m^2. It could be seen from Table 3 that when the applied AC stray current density was less than 100 A/m^2, the Tafel slope ratio changed from greater than 1 to less than 1; it indicated that the corrosion process was controlled from anode control to cathode control. When the applied AC stray current density was more than 200 A/m^2, the Tafel slope ratio was always less than 1; it indicated that the corrosion process was always controlled by the cathode. And the greater the applied AC stray current density, the more prone to cathode control.

3.3. Electrochemical Impedance Spectroscopy. In order to further research the influence of the AC density on the corrosion behavior of X80 pipeline steel under the disbonded coating defects, the electrochemical impedance spectroscopy of X80 steel under different AC stray current density interference was tested. The results are shown in Figure 10.

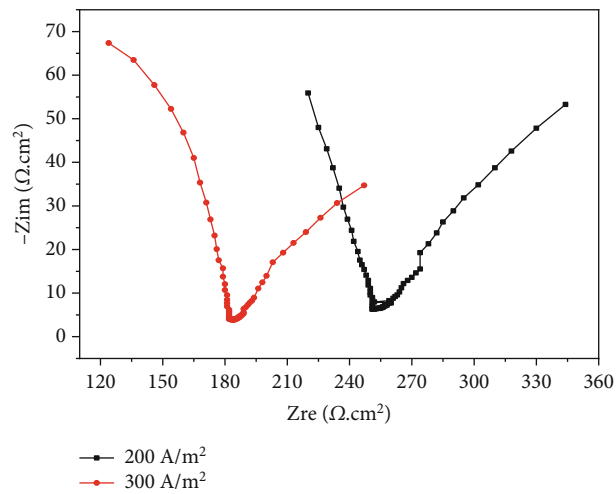

Figure 11: Electrochemical impedance spectroscopy on the ninth day under high AC density.

Table 4: R value of X80 steel under disboned coating with different AC density interference.

AC density (A/m^2)	Time (d)	R_t (Ω)	Time (d)	R_t (Ω)
	0	60.9	5	141.9
0	1	116.6	7	123.1
	3	113.4	9	74.8
	0	119.5	5	171.9
30	1	167.6	7	153.6
	3	237.2	9	120.2
	0	117.2	5	220.4
50	1	153.7	7	214.4
	3	164.4	9	180.4
	0	203.9	5	270.6
100	1	227.1	7	258.3
	3	246.8	9	206.0
	0	215.5	5	253.5
200	1	237.2	7	248.4
	3	243.4	9	307.1
	0	183.3	5	332.0
300	1	246.6	7	304.2
	3	183.4	9	262.3

It could be seen from Figure 10 that under the action of low AC density, the EIS characteristics of X80 steel showed a capacitive antiarc in the early stage, and there were no obvious inductive resistance and diffusion characteristics. This shows that at the beginning of the experiment, uniform corrosion occurred on the metal surface under the interference of low AC current density. With the application of alternating current interference, an inductive arc occurred, which might be related to the adsorption or peeling of corrosion products. Under the action of high current density, the EIS characteristics of X80 steel showed capacitive and antiarc in the early stage, and there were no obvious inductive resistance and diffusion characteristics. As the test progressed,

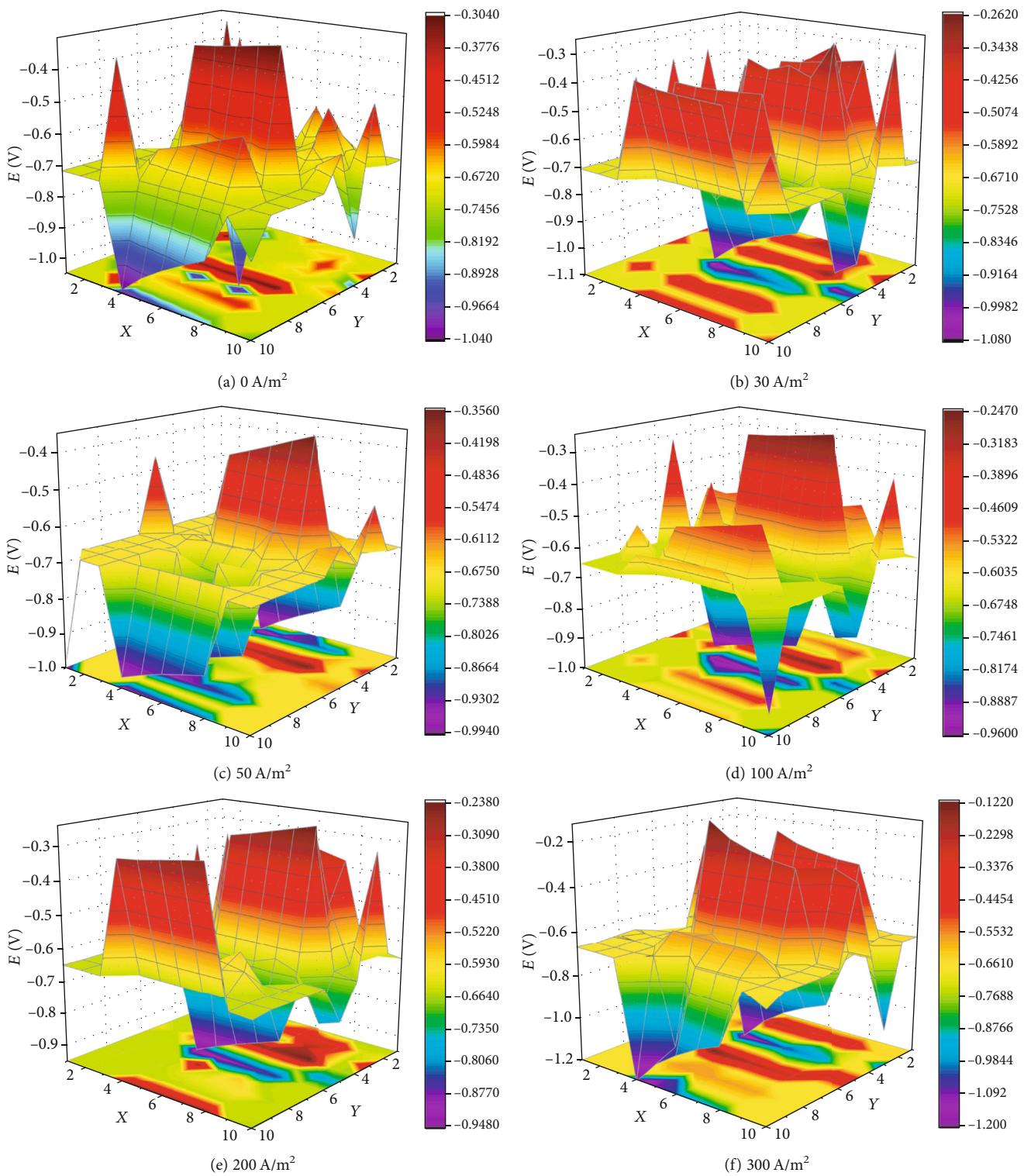

Figure 12: Array electrode potential distribution at different AC densities.

the low-frequency impedance spectrum showed the Warburg impedance, which was proportional to the current density of the AC interference, as shown in Figure 11. Under different AC density interferences, the diffusion impedance at high AC density was greater than at low current density. Under different AC density interferences, the diffusion impedance at high AC current density was greater than at low current density. Under the action of high AC current density, the metal outside the gap was seriously corroded and caused corrosion products to accumulate at the edge of the gap, which was the reason for the diffusion impedance.

The electrochemical impedance spectrum was fitted with the equivalent circuit diagram. In order to ensure that the error rate was within the controllable range, different circuit diagrams

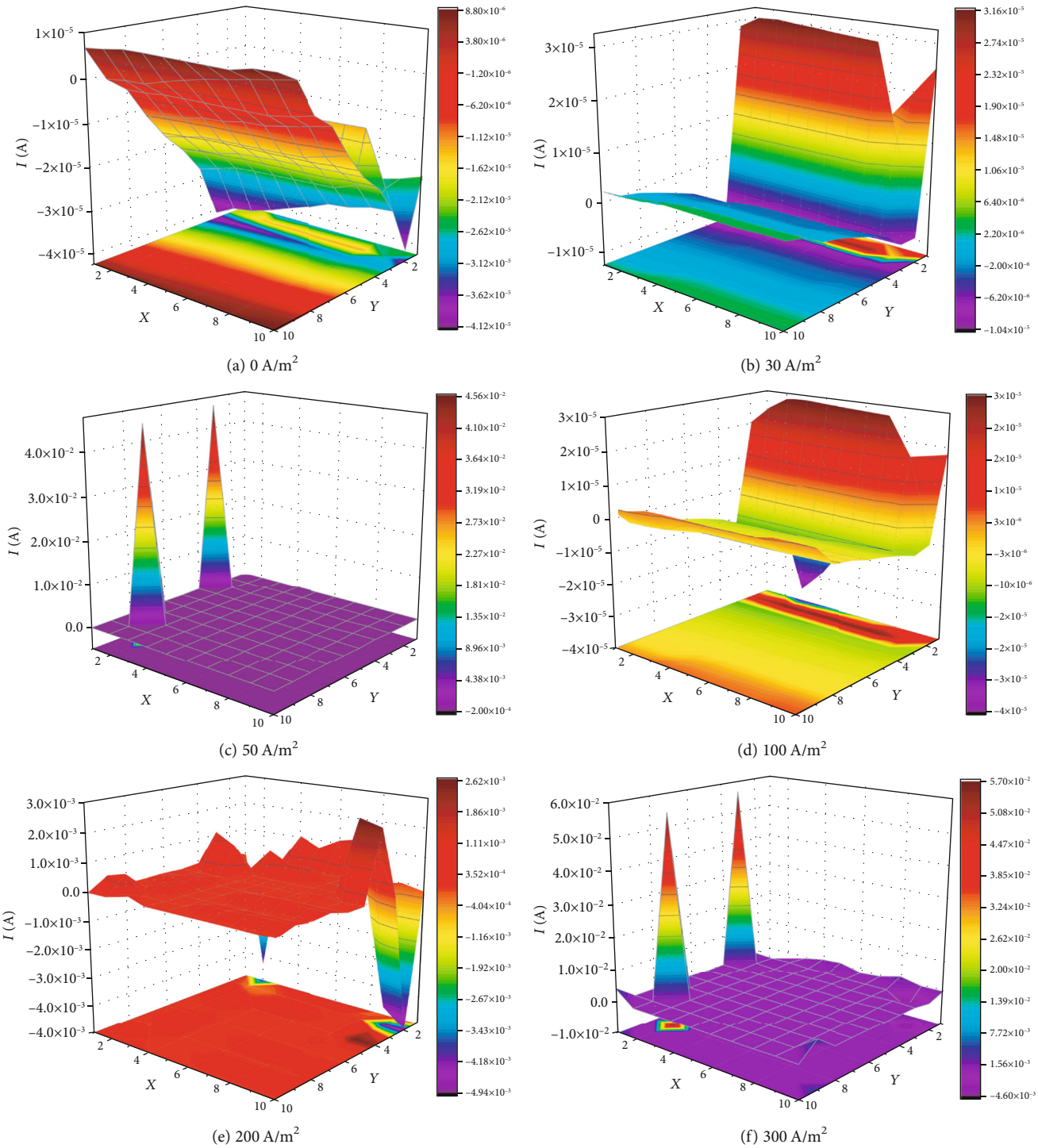

Figure 13: Array electrode current distribution at different AC densities.

were selected for different electrochemical impedance spectra. For the AC impedance with the sense of antiarcing, the equivalent circuit ($C(R_t(\mathrm{LR}))$) was selected. The AC impedance with the Warburg impedance was fitted with the equivalent circuit $R(C(R_t W))$, which the rests were fitted with the equivalent circuit ($C(R_t(\mathrm{CR}))$). R_t was a charge transfer resistance. According to the electrochemical principle, the larger value of R_t, the better the corrosion resistance of electrode. The fitting results of the charge transfer resistance of X80 steel under the influence of different AC density are shown in Table 4.

It could be seen from Table 4 that the R_t value at the beginning was the smallest when no AC stray current interference was applied. It indicated that the corrosion current density that was the largest at the beginning was the smallest when no AC stray current interference was applied. As the test progressed, the R_t value first increased and then

decreased. Compared with Figure 9, it was found that the corrosion current density first decreased and then increased, that was, when the charge transfer resistance value was large, the corrosion current density was relatively small. Comparing the R_t value and the corrosion current density value in the other cases, a similar law was found.

3.4. WBE Measurement. The measured electrode potential and current of the X80 steel array electrode under different AC densities after 9 days of experiment are shown in Figures 12 and 13.

It could be seen from Figures 12(a) and 13(a) that the potential X80 steel outside the gap was proportional to the potential inside the gap, which range was from -0.30 V to -1.04 V. The current distribution on the 9th day of the experiment was similar to the 5th day of the experiment. The cathode region was still expanding toward the inside of the gap, and an anode current appeared only at the 10th row of the array electrode. It indicated that the anode of the metal was always dissolved at the bottom of the gap.

It could be seen from Figures 12(b) and 13(b) that the potential outside the gap and the bottom of the gap was the potential inside the gap, which range was from -0.26 V to -1.08 V. There is an anode current at the edge of the gap (the second row), and there was a large area of negative current inside the gap. There is anode current at the bottom of the gap and at the edge of the gap (line 2), while there is a large area of cathode current inside the gap. The metal at the bottom of the gap is still in the anode zone, where metal corrosion reaction is taking place.

It could be seen from Figures 12(c) and 13(c) that the positive potential only appeared in the fourth row of the array electrode, and the potential in the other regions was more negative, which range was from -0.36 V to -0.99 V. The cathode current appeared only on several array point electrodes outside the gap and at the edge of the gap. The local maximum anode current that appeared at points (1–3, 8) was 4.55×10^{-2} A, while the anode current in the surrounding area was on the order of 10^{-5} A; it indicated that at the two points, severe localized corrosion has occurred.

It could be seen from Figures 12(d) and 13(d) that the potential outside the gap and the bottom of the gap was proportional to the potential inside the gap, which range was from -0.25 V to -0.96 V. The second row (slit edge) of the array electrode and the ninth and tenth rows (the bottom of the slit) were anode currents, and the remaining regions were the cathode currents, which accelerates the corrosion of the local anode region at the bottom of the gap.

According to Figures 12(e) and 13(e), the negative potential was distributed in the middle of the gap, which range was from -0.24 V to -0.95 V. There was an anode current at the points (1–3, 8) of up to 5.69×10^{-2} A. It indicated that severe localized corrosion has occurred there, while anode currents in other regions were relatively small. The cathode current is only produced on four array point electrodes outside the gap and at the edge of the gap. Compared with Figures 12(c) and 13(c), the area of the anode region was further enlarged, and local corrosion was more serious.

According to Figures 12(f) and 13(f), the potential distribution range was from -0.12 V to -1.20 V, which distributed between phases. At the same time, the external potential of the gap was at the potential inside the gap. The cathode current was only generated at a part of the array electrodes outside the gap and at the edge of the gap, while the other regions were dominated of the anode current. At this time, no large anode current appeared and the distribution was relatively uniform.

In summary, with the progress of the experiment, the potential difference at each point on the surface of the array electrode was gradually reduced. In the later stage of the experiment, the potential difference of X80 under different AC densities was not much different, and the rang was from 0.36 V to 1.08 V. When the AC density was 50 A/m^2 and 200 A/m^2, two local maximum anode currents appeared at the array electrode, which were of the order of 10^{-2} A. In other cases, when the AC density was less than 100 A/m^2, the cathode current zone and the anode current zone were more clearly separated, and the anode current was on the order of 10^{-5} A; it indicated that the degree of corrosion was not much different. As the density of the applied AC increased, the electrode current of the array electrode gradually increased, and the area of the anode region gradually increased. It was indicated that under the action of the autocatalytic effect of the oxygen concentration cell and the occlusion cell, the metal inside the gap was always in an accelerated dissolution state, and the existence of AC interference enhanced the activity of the metal and was more conducive to the occurrence of corrosion. When the AC stray current density was 300 A/m^2, the magnitude of the anode current was about 100 times that of the case where no AC interference was applied, which was sufficient to explain the influence of AC interference on the metal corrosion under the disbonded coating.

4. Conclusion

(1) AC interference caused the Eocp of X80 steel to shift. As the AC density increased, the Eocp fluctuation amplitude and the negative offset increased

(2) The presence of AC accelerated the corrosion process of X80 steel. The higher the AC intensity, the faster the corrosion rate. As corrosion occurred, the accumulation and attachment of corrosion products could affect the diffusion of oxygen and reduced the corrosion rate

(3) It could be seen from the measurement results of WBE that the surface potential distribution of the array electrode was not uniform, but the overall rule was that the external potential of the gap was more positive than that inside the gap. Under the action of the autocatalytic effect of the oxygen concentration cell and the occlusion cell, the cathode region was mainly distributed on the outer and edge of the gap, and the anode region was mainly distributed inside the gap

Data Availability

The data used to support the findings of this study are included within the article.

Disclosure

The funders had no role in the design of the study and collection, analysis, and interpretation of data and in writing the manuscript.

Conflicts of Interest

The authors declare that there is no conflict of interest regarding the publication of this article.

Acknowledgments

We would like to thank Miss Xiaoyu Shi for her assistance in the experiments. This work was supported by the basic scientific research service fee of the Central University of Civil Aviation University of China (3122019107).

References

[1] D. S. Mu, G. Fu, and X. Q. Chen, "Oil and gas leakage positions of fault cap rock configuration and its control on hydrocarbon accumulation of Ng3 in Nanpu 1 structure area," *Jilin Daxue Xuebao (Diqiu Kexue Ban)/Journal of Jilin University (Earth Science Edition)*, vol. 48, no. 4, pp. 1008–1017, 2018.

[2] Y. Wang and K. J. Karisallen, "Physical scale modelling of stray current interference to shipboard ICCP system," *British Corrosion Journal*, vol. 52, no. 3, pp. 212–219, 2017.

[3] L. Bertolini, M. Carsana, and P. Pedeferri, "Corrosion behaviour of steel in concrete in the presence of stray current," *Corrosion Science*, vol. 49, no. 3, pp. 1056–1068, 2007.

[4] Y. I. Kuznetsov, A. D. Mercer, and J. G. N. Thomas, "Electrochemical aspects of the inhibition of corrosion of metals," in *Organic Inhibitors of Corrosion of Metals*, 1996.

[5] B. Vuillemin, R. Oltra, R. Cottis, and D. Crusset, "Consideration of the formation of solids and gases in steady state modelling of crevice corrosion propagation," *Electrochimica Acta*, vol. 52, no. 27, pp. 7570–7576, 2007.

[6] B. Mccollum and G. H. Ahlborn, "The influence of frequency of alternating or infrequently reversed current on electrolytic corrosion," *Proceedings of the American Institute of Electrical Engineers*, vol. 182, no. 1, pp. 108–110, 2013.

[7] S. Pookote and D. Chin, "Effect of alternating current on the underground corrosion of steels," *Materials Performance*, vol. 17, no. 3, pp. 9–15, 1978.

[8] R. Liu and C. F. Li, "Determinate dimension of numerical simulation model in submarine pipeline global buckling analysis," *Ocean Engineering*, vol. 152, pp. 26–35, 2018.

[9] L. A. de Oliveira, O. V. Correa, D. J. dos Santos, A. A. Z. Páez, M. C. L. de Oliveira, and R. A. Antunes, "Effect of silicate-based films on the corrosion behavior of the API 5L X80 pipeline steel," *Corrosion Science*, vol. 139, pp. 21–34, 2018.

[10] E. S. Ouellette, A. A. Shenoy, and J. L. Gilbert, "The seating mechanics of head-neck modular tapers in vitro: load-displacement measurements, moisture, and rate effects," *Journal of Orthopaedic Research*, vol. 36, no. 4, 2017.

[11] Z. Ahmad, *Principles of Corrosion Engineering and Corrosion Control*, 2006.

[12] H. W. Pickering, "The significance of the local electrode potential within pits, crevices and cracks," *Corrosion Science*, vol. 29, no. 2-3, pp. 325–341, 1989.

[13] R. E. Williford Jr., C. F. Windisch Jr., and R. H. Jones, "In situ observations of the early stages of localized corrosion in type 304 SS using the electrochemical atomic force microscope," *Materials Science & Engineering A (Structural Materials: Properties, Microstructure and Processing)*, vol. 288, no. 1, pp. 54–60, 2000.

[14] L. T. Huo, *Corrosion behaviors of X70 pipeline steels with coating holidays*, Inner Mongolia University of Science & Technology, 2007.

[15] M. C. Yan, J. Q. Wang, and E. H. Han, "Characteristics and evolution of thin layer electrolyte on pipeline steel under cathodic protection shielding disbonded coating," *Acta Metallurgica Sinica*, vol. 50, no. 9, pp. 1137–1145, 2014.

[16] C. Wen, J. Li, S. Wang, and Y. Yang, "Experimental study on stray current corrosion of coated pipeline steel," *Journal of Natural Gas Science and Engineering*, vol. 27, no. 3, pp. 1555–1561, 2015.

[17] M. Zhu, Y. Yuan, Q. Zhang, S. Yin, and S. Guo, "Influence of AC interference on crack initiation behavior of pipeline steel in high pH solution," *International Journal of Electrochemical Science*, vol. 14, no. 1, pp. 1876–1883, 2019.

[18] R. W. Bosch and W. F. Bogaerts, "Harmonic analysis of corroding systems considering diffusion phenomena," *Journal of the Electrochemical Society*, vol. 143, no. 12, 1996.

[19] X.-H. Wang, Z.-Q. Wang, Y.-C. Chen, X.-T. Song, and C. Xu, "Effects of stray AC interference on corrosion behavior of X70 pipeline steel in a simulated marine soil solution," *International Journal of Electrochemical Science*, vol. 12, no. 3, pp. 1829–1845, 2017.

[20] Y. Li, Q. Li, X. Tang, and Y. Li, "Reconstruction and characterization of galvanic corrosion behavior of X80 pipeline steel welded joints," *Acta Metallurgica Sinica*, vol. 55, no. 6, pp. 801–881, 2019.

[21] Z. P. Zhao, G. Y. Qiao, and G. P. Li, "Fatigue properties of ferrite/bainite dual-phase X80 pipeline steel welded joints," *Science and Technology of Welding & Joining*, vol. 22, no. 3, pp. 1–10, 2016.

[22] Z. Magdalena, P. Miloslav, and K. Petr, "Determination of chromium in the surface nano-layer covering the Zn-based anti corrosion coating of steel sheets using a laser-induced breakdown spectrometry," *Chemical Papers*, vol. 71, no. 11, pp. 2045–2052, 2017.

[23] J. Chen, J. Wu, P. Wang, D. Zhang, S. Chen, and F. Tan, "Corrosion of 907 steel influenced by sulfate-reducing bacteria," *Journal of Materials Engineering and Performance*, vol. 28, no. 3, pp. 1469–1479, 2019.

[24] F. Long, W. Cheng, G. Chen et al., "Corrosion fatigue properties of AZ21 Mg alloy under different cyclic loading conditions," vol. 38, no. 10, pp. 1635–1641, 2017.

[25] S. Xu, F. F. Xing, W. Li, Y. Q. Wang, and R. L. Wang, "A stray current sensor based on an all-side cylindrical spiral fiber," *IEEE Photonics Journal*, vol. 9, no. 1, pp. 1–14, 2017.

[26] M. D. Paz, D. Zhao, S. Karlsson, J. Liske, and T. Jonsson, "Investigating corrosion memory: the influence of previous boiler operation on current corrosion rate," *Fuel Processing Technology*, vol. 156, pp. 348–356, 2017.

[27] T. Chuchit and T. Kulworawanichpong, "Stray current assessment for DC transit systems based on modelling of earthing and bonding," *Electrical Engineering (Archiv fur Elektrotechnik)*, vol. 101, no. 1, pp. 81–90, 2019.

[28] X. Zhang, J. Zhang, N. Dai et al., "Probing the corrosion mechanism of zinc under direct current electric field," *Materials Chemistry and Physics*, vol. 206, pp. 232–242, 2018.

[29] C. A. Charalambous, "Comprehensive modeling to allow informed calculation of DC traction systems' stray current levels," *IEEE Transactions on Vehicular Technology*, vol. 66, no. 11, pp. 9667–9677, 2017.

[30] L. Javier, M. Christian, and Á. M. Jesús, "On the assimilation set-up of ASCAT soil moisture data for improving streamflow catchment simulation," *Advances in Water Resources*, vol. 111, pp. 86–104, 2018.